Geometry-Based Customization of Bending Modalities for 3D-printed Soft Pneumatic Actuators

Luca Rosalia[1], Benjamin Wee-Keong Ang[2], and Raye Chen-Hua Yeow[3]

Abstract— **In this work, we propose a novel type of 3D-printed soft pneumatic actuator that allows geometry-based customization of bending modalities. While motion in the 3D-space has been achieved for several types of soft actuators, only 2D-bending has been previously modelled and characterized within the scope of 3D-printed soft pneumatic actuators. We developed the first type of 3D-printed soft pneumatic actuator which, by means of the unique feature of customizable cubes at an angle with the longitudinal axis of the structure, is capable of helical motion. Thus, we characterize its mechanical behavior and formulate mathematical and FEA models to validate the experimental results. Variation to the pattern of the inclination angle along the actuator is then demonstrated to allow for complex 3D-bending modalities and the main applications in the fields of object manipulation and wearable robotics are finally discussed.**

Index Terms— **Grippers and Other End-Effectors; Hydraulic/Pneumatic Actuators; Rehabilitation Robotics**

I. Introduction

Advances in material science have led to a myriad of structures and principles that made soft robotics actuators capable of several types of motion. Shape memory alloy (SMA) and shape memory polymer (SMP) actuators, which are activated by thermal or electrical stimuli, can create complex geometries including 3D-bending and helical motion [1], but their performance is limited due to a narrow range of usable strain, a low actuation frequency, and a relatively low controllability, accuracy, and energy efficiency [2]. Dielectric elastomer actuators (DEA) are a different class of actuators based on electroactive polymers, which are typically sandwiched between two electrodes and deform mechanically upon variations of the electric field [3]. While they are mostly restricted to 2D-bending [4], the improved single-body dielectric elastomer actuators (SDEA) can also perform more complex movements such as helical motion [5]. However, manual fabrication prevents miniaturization of the devices and is time-consuming with limited reproducibility [6]. Furthermore, the high voltage required for operation precludes them from medical applications in wearable robotics [7].

Within the scope of soft pneumatic actuators (SPA), although most research has been focusing on extension [8], compression [9] [10], and bending actuators [11], twisting [12] and helical motion [13] pneumatic actuators have been only marginally investigated. Fiber-reinforced actuators are a particular type of silicon-based SPAs which are capable of achieving a multiplicity of motion types, including bending, extension, and twisting, by simply varying the geometry of the fiber reinforcements of the elastomeric matrix, which effectively programs the motion of the actuator [14] [15]. Due to the variety of motion types, the low cost, their compliance and flexibility, and their relatively high force output, fiber-reinforced actuators and other types of SPAs have been broadly developed. Furthermore, due the compatibility of the force output with most joints in the human body, these actuators have been widely utilized for human rehabilitation purposes. However, manufacturing fiber-reinforced actuators involves numerous steps, it is hugely dependent on the user's skills, and is considerably time- and resource-intensive.

Rapid prototyping, customizable design, and single-step fabrication of complex structures at high resolutions are the main advantages of 3D-printing of flexible materials [16] over manual fabrication of elastomeric material via mold-casting. Actuators made of flexible materials using 3D-printers based on fused deposition modelling (FDM) technology have been made capable of performing extension and bending motion and achieving high force output [17] [18]. Although combination of 3D-printing of flexible materials such as NinjaFlex with other materials (e.g. fabric) has broadened the attainable range of motion by allowing heterogeneous bending trajectories [19], the motion of such actuators is still limited to a planar bending profile. Nevertheless, the potentials of 3D-printed actuators to perform helical motion have been recently demonstrated [18]. However, the actuator that was developed remained wanting in characterization of the kinematics in the

Manuscript received: February, 2, 2018; Revised: May, 22, 2018; Accepted: June, 27, 2018.

This paper was recommended for publication by Paolo Rocco upon evaluation of the Associate Editor and Reviewers' comments.

[1] Mr. Luca Rosalia is with the School of Engineering, University of Glasgow, and the Department of Biomedical Engineering, National University of Singapore (email: luca.rosalia95@gmail.com)

[2] Mr. Benjamin Wee-Keong Ang is with the Department of Biomedical Engineering, National University of Singapore (email: benjamin_angwk@yahoo.com.sg).

[3] Dr. Raye Chen-Hua Yeow is with the Department of Biomedical Engineering, National University of Singapore, the Advanced Robotics Centre, and the Singapore Institute for Neurotechnology (e-mail: rayeow@nus.edu.sg).

3D-space due to the undesired bending of the proximal end of the structure.

This study proposes a novel design for 3D-printed SPAs which features customizable cubes at an angle with the longitudinal axis of the actuator. Variation of such angle and of the frontal and back surface areas of customizable cubes results in several types of 3D-bending modalities. We therefore fully characterize the mechanical behavior of the developed actuator in the 2D- and 3D-space and demonstrate the flexibility of the design for a number of other 3D-bending modalities. It follows investigation of possible applications in the fields of object manipulation and soft wearable devices for rehabilitation. Particularly, we demonstrate that, for closely conforming to the path of the thumb joint, the helical motion achieved by our proposed actuator could aid in rehabilitation of the thumb allowing for opposition. This constitutes an important contribution to 3D-printed soft wearable devices for hand rehabilitation, which are currently restricted to mere extension and flexion of the digits by means of 2D-bending actuators.

II. Materials and Methods

A. Design and fabrication

As illustrated in Fig. 1(a-b), our proposed 3D-printed SPA consists of customizable cubes which form an angle with the strain limiting layer of the bottom aspect of the actuator. The air channel shown in Fig. 1(c) passes from the inlet to the cubes through hollow segments at the base running between the two opposing faces of each pair of adjacent cubes. Unlike other comparable designs exploiting the fold-based actuation mechanism [18], the unique feature of the inclination angle between the anterior or posterior faces of each cube and the frontal axis allows, when air pressure is applied, not only for bending on the longitudinal plane, but also on the frontal plane. This results into a 3D-bending, or helical, profile. It should be noted that the term twisting is unbecoming in this context in that the longitudinal axis of the resulting helix is not coincident with that of the actuator. As explained in the sections below, the inclination angle of the cubes and the surface area of the frontal and back faces are the main features upon which the motion of the actuator is dependent.

The actuators were designed using CAD software (Dassault System SOLIDWORKS Corp, MA) and the model files imported to a free open-source software, Cura (Ultimaker B.V., Geldermalsen, Netherlands) to control the printing parameters, and generate the G-code for the LulzBot TAZ 6 (Aleph Objects Inc, CO) printer. The printing material used was thermoplastic elastomer filament NinjaFlex (NinjaTek, PA), and the actuators were printed sideways to simplify the printing process by minimizing overhang and thus reduce the risk of air leakage upon pressurization [17].

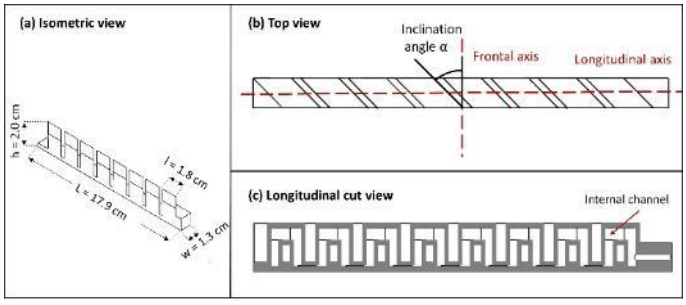

Figure 1. (a) Isometric, (b) top, and (c) longitudinal cut view of an 8-cube actuator with inclination angle α = 45° and dimensions (17.9 x 1.3 x 2.0) cm.

B. Material characterization methods

In order to derive the constitutive equation of the stress-strain response of Ninjaflex, uniaxial tensile testing was conducted on five standard 3D-printed dog-bone-shaped specimens (ISO 7743) made of Ninjaflex using an Instron (model 3345) single column table-top electromechanical tester. The operational range of the curve, which was set to be from 0-100% strain, was fitted (R^2 = 0.9994 ± 0.0007) using the 3rd order Yeoh model in (1) [20] [21]. Fitting outside the operational range would result in a less accurate estimate of the Yeoh coefficients: for instance, fitting to 0-500% strain would yield R^2 = 0.9729 ± 0.0034.

$$\sigma = \sum_{i=1}^{N=3} 2 * C_i * i * (\lambda - \lambda^{-2}) * (I_1 - 3)^{i-3}, \quad (1)$$

where σ and λ are the engineering stress (MPa) and stretch ratio respectively, I_1 is the first deviatoric strain invariant, and $C_{1\text{-}3}$ are the material-specific coefficients.

C. Experimental methods

The kinematics of the actuator was characterized using Vicon MX system (Oxford Metrics, UK), a high accuracy optical tracking system [22] [23] widely utilized for gait analysis purposes [24] [25] or other robotic applications [26]. By securing small and lightweight retroreflective markers on the superior surface of four of the customizable cubes, the position of the actuator could be recorded. Each of the actuators was then clamped using a retort stand ensuring that the motion of the actuator on the x-y plane would trace a circle as illustrated in Fig. 2(a-b). Hence, a circle was fitted through the position of the markers, and the mean radial percentage error was calculated for each measurement as in (2):

$$\varepsilon = \frac{\sum_{i=1}^{N} |R_i - R_{fit}|}{N} * \frac{100}{R_{fit}} \%, \quad (2)$$

where R_i and R_{fit} are the experimental radii at each point and the fitted radius respectively, and N is the number of markers used. Therefore, each trial was considered successful if the maximum error did not exceed 5% of the radius and the average error did not exceed 2.5%.

Eighteen readings were taken under static conditions from 0kPa to 340kPa in steps of 20kPa and each trial was repeated three times. The angular displacement of the two ends of the actuator and the bending radius, or that of the helix, could therefore be calculated.

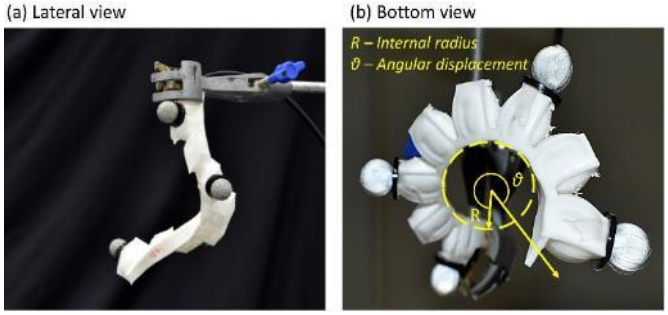

Figure 2. (a) Lateral and (b) bottom view of experimental setup, with internal radius and angular displacement labelled.

The force applied by the actuator was characterized via blocked force measurements. The test was performed placing a force sensitive resistor (FSR) on the inferior aspect of the actuator, whose motion was entirely constrained by plastic plates on the lateral and superior sides of the structure, and continuously increasing the pressure from 0kPa to 300kPa. Each measurement was repeated three times for averaging.

III. Modelling

The 2D- and 3D-bending capabilities of the developed actuators were investigated by means of mathematical and FEA modelling. These models were used for validation of the experimental results as outlined in the sections below.

A. 2D-bending

If the customizable cubes are aligned with the longitudinal axis of the actuator, bending of the base segments connecting adjacent cubes upon pressurization causes planar bending of the actuator. Indeed, as shown in Fig. 3, bending of each segment occurs along the perpendicular direction to the front and back faces of each customizable cube. Each of these faces can be modelled as a rectangular plate with all edges fixed and a uniformly distributed load, whose maximum deflection and stresses can be calculated using 3(a-c) [27] [28] [29] [30]:

$$y_{max} = \frac{\alpha q b^4}{Et^3}, \tag{3.a}$$

$$\sigma = \frac{\beta_2 q b^2}{t^2} \ (at\ centre), \tag{3.b}$$

$$\sigma = \frac{-\beta_1 q b^2}{t^2} \ (at\ centre\ of\ long\ edge), \tag{3.c}$$

where q is the pressure applied, b and t are the smaller side and the thickness of the plate respectively, E is the Young's Modulus, and α and β are coefficients that vary with the ratio of the length of the two sides of the plate. Given a measure of the stress, an estimate of the Young's Modulus as a function of pressure could be obtained from the Yeoh model. Assuming the stress distribution on each face to be radial due to the symmetry of the boundaries, the mean deflection across the frontal cross-section can be calculated from the mean value theorem. Finally, assuming that the front and back faces of each cube remain perpendicular to the Neutral Axis, the bending angle can be calculated for N customizable cubes as in (4):

$$\vartheta_{bending} = 2 * (N-1) * \arctan(\frac{y_{mean}}{d_{NA}}), \tag{4}$$

where d_{NA} is the distance between the point of maximum deformation and the Neutral Axis.

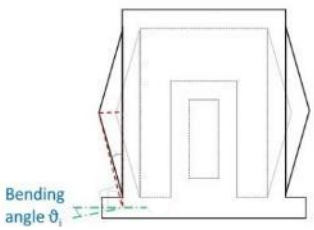

Figure 3. Bending of a single cube from pressurization of the internal channel.

B. Helical motion

If the direction of the normal to the front and back faces of the customizable cubes is not that of the longitudinal axis of the actuator, the bending profile is that of a helix. A similar model of a uniformly loaded plate as that previously outlined can be used to expound the helical motion of these actuators. However, in this case, the edge of the plate that forms an obtuse angle between the lateral and front (or back) faces of each customizable cube, is no longer a valid boundary as it is subjected to non-zero deflection. Instead, for undergoing zero deflection, the intersection of such edge with the walls of the internal channel can be considered the new boundary of the plate. The other three boundaries, namely the top and bottom edges, and the lateral edge on the side of the acute angle remain unaltered. Due to the asymmetry of the boundaries, the stress distribution is skewed towards the edge on the side of the obtuse angle. Therefore, assuming that the angle between the new axis of the deflection profile and the vertical is the same as the angle at which the plate is inclined, the maximum deflection can be approximated for any inclination angle α_{incl} as in (5), and the angular displacement computed using the mean value theorem similarly to the 2D-bending case.

$$y_{\max} = \frac{\alpha q b^4}{Et^3 \cos(\alpha_{incl})}. \tag{5}$$

Finally, the bending radius or the inner radius of the helix can be calculated given that the circumference described is the projection of the actuator of length l onto the plane perpendicular to the axis of the helix, yielding the result in (6):

$$r(p,\alpha) = \frac{360}{\theta(p,\alpha)} * \frac{l}{2\pi}\cos\alpha, \tag{6}$$

where θ is the bending angle or angular displacement, and p and α are the actuation pressure and the inclination angle respectively. In the particular case when α = 0, (6) gives the bending radius of a simple 2D-bending profile.

C. Finite Element Modelling

The kinematic behavior of the actuators was further investigated with Finite Element Modelling using ABAQUS/CAE (Simulia, Dassault Systemes, RI). Pneumatic pressure (p = 340kPa) was applied to all the internal surfaces of the actuators. The hyperelastic behavior of the material was modelled using the Yeoh coefficients obtained as described above. All the actuators were meshed using solid tetrahedral quadratic hybrid elements, and the boundary conditions of a built-in beam were applied to the proximal end.

Fig. 4(a-c) illustrates the change in the stress and deflection distribution profiles of the frontal surface of each customizable cube for changes of the inclination angle. In accordance with the physical model, the maximum stress and the maximum deflection increase with α, and the profile is skewed towards the obtuse angle. Fig. 4(d) demonstrates that, for actuators capable of helical motion, the deflection is not zero at the edge forming the obtuse angle, but it is at the intersection with the walls of the internal channel, which further validates the plate theory and the assumptions used in the physical model. Finally, Fig. 4(e-f) shows the bending and helical deformation profiles for α = 0° and 45° at different actuation pressure values.

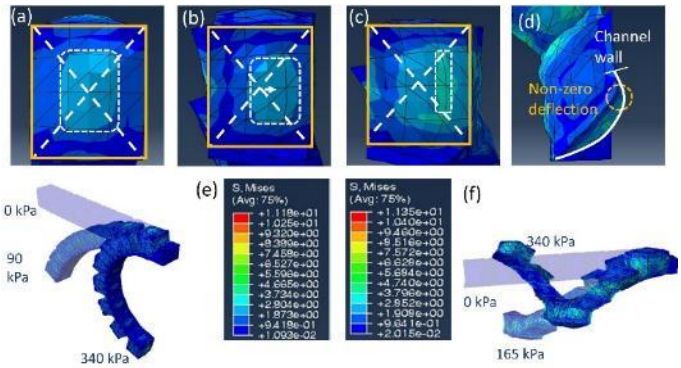

Figure 4. FEA stress and deflection distribution profiles for (a) α=0°, (b) α=25°, and (c) α=45° at p = 340kPa. (d) Deflection profile of an actuator capable of helical motion (α=45° at p = 340 kPa). Deformation profile of (e) a bending actuator at p = 0, 90, 340 kPa and (f) of an actuator capable of helical motion (α=45°) at p = 0, 165, 340 kPa.

IV. Characterization

The mechanical behavior of the actuators was investigated varying different geometrical parameters, namely the inclination angle and the width of the front and back faces of the cubes. The angular displacement and the internal radius of the actuators upon pressurization were measured to understand the motion kinematics, while the output force was obtained by means of a blocked force test.

A. 2D-bending

The bending angle of the 2D-bending actuator was first measured upon pressurization. Experimental data show to be closely comparable with both the mathematical and finite element models. Results, which are illustrated in Fig. 5(a-b), demonstrate a linear relationship between pressure and bending angle, while a rapid decay of the internal radius with increasing pressure can be observed.

B. Helical motion: inclination angle

The angular displacement of actuators capable of helical motion was measured for four different inclination angles, namely 25°, 35°, 45°, 55°. In varying the geometry, the surface area of each face of the cubes was kept constant, along with the height, the length, and the number of customizable cubes. The experimental results, which are depicted in Fig. 6 together with the mathematical and finite element models, show that the angular displacement increases with pressure and with the inclination angle. Contrarily, the internal radius of the helix decreases with both pressure and inclination angle. Although the error between the experimental results and the mathematical and FEA models is slightly larger than for the 2D-bending analysis, similar relationships between the aforementioned variables could be confirmed.

C. Helical motion: cube side length

The kinematic capabilities of the proposed design were further assessed upon variations of the dimensions of the customizable cubes. For this purpose, the width of the front and back faces of each cube were varied (l = 0.75cm, l = 1.5cm, l = 3.0cm) and measures of the angular displacement and the internal radius obtained. In this experiment, all the other geometrical parameter of the design were kept constant and all the actuators had an inclination angle of α = 45°. As shown in Fig. 7, at a given pressure, the angular displacement is larger for wider actuators. However, while a negligible change in internal radius was experimentally observed for different values of l, both the physical model and the FEA predict a decrease in the internal radius of the helix for increasing values of l. It should be noted that doubling of the weight of the actuator as a result of the doubled width (l = 3.0cm) magnifies the difference between experimental results and the mathematical and finite element models. This, together with inappreciable movements of the stand to which the actuators are clamped and its inclination, constitutes the main source of error.

D. Blocked force test

In order to predict the behavior of the actuator under payloads, which is paramount to ensure controllability, a

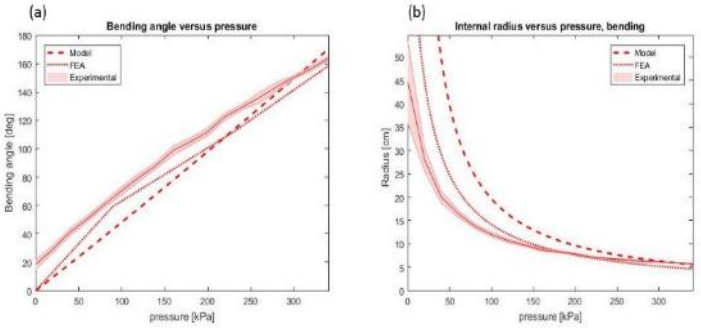

Figure 5. (a) Bending angle, and (b) internal radius versus pressure for bending actuators.

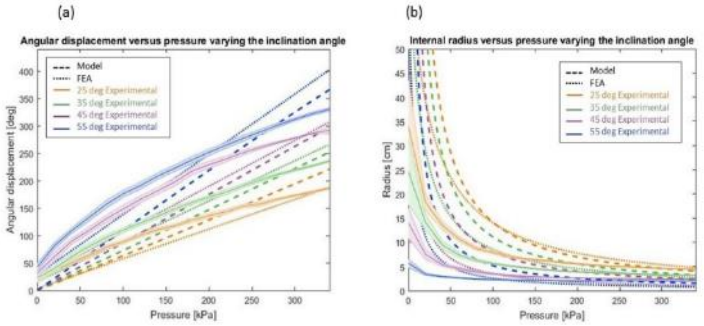

Figure 6. (a) Angular displacement and (b) internal radius versus pressure varying the inclination angle of actuators capable of helical motion.

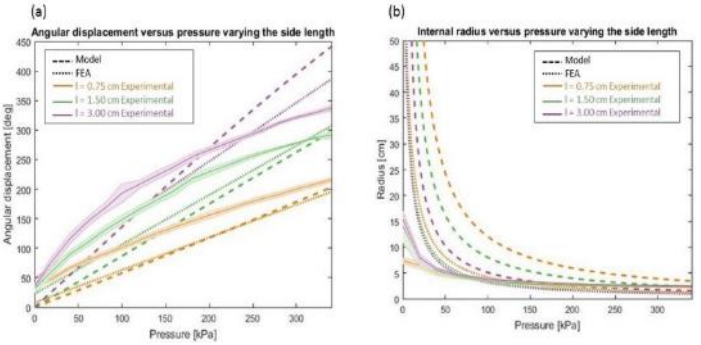

Figure 7. (a) Angular displacement and (b) internal radius versus pressure varying the side length of actuators capable of helical motion.

blocked force test was performed. This was carried out measuring the output force in full motion constraint.

For this purpose, four designs were investigated varying the inclination angle and the length of the cube side. Thus, the output force was measured for pressures up to 300 kPa for one 2D-bending actuator ($\alpha = 0^o$) and two actuators capable of helical motion ($\alpha = 25^o$, $\alpha = 45^o$) with $l = 1.5$cm, and one actuator capable of helical motion ($\alpha = 45^o$) with $l = 3.0$cm. The graph in Fig. 8 shows the output force versus the angular displacement as obtained upon mapping of the actuation pressure by means of the kinematics analysis described above. This effectively provides a measure of the maximum force that actuators can withstand at a given position. Firstly, it should be noted that, albeit marginally, the output force depends on the inclination angle of the cubes as it is greater for larger values of α. Secondly, increasing the length of the cube edge, thus the width of the actuator, augments the output force, the difference being most significant at high pressure. Therefore, the width of the front and back faces of the actuator can be tuned to achieve different output forces at a given position.

E. Design variations

Aside from the helical motion that has been characterized, the actuator presented in this work is capable of achieving a variety of motion profiles in the 3D-space by solely varying the configuration of the inclination angle of the cubes. Three variations to the design were made to show customizability. The prototypes shown in Fig. 9 and summarized below were manufactured by fixing all the other geometrical parameters.

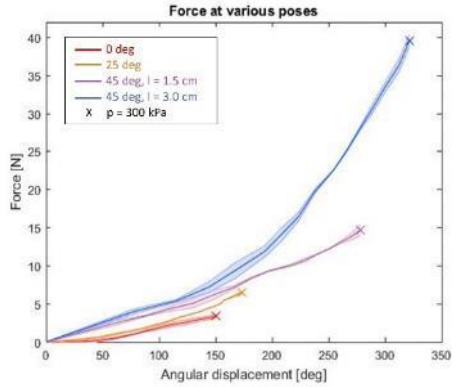

Figure 8 – Output force at various poses from blocked force test.

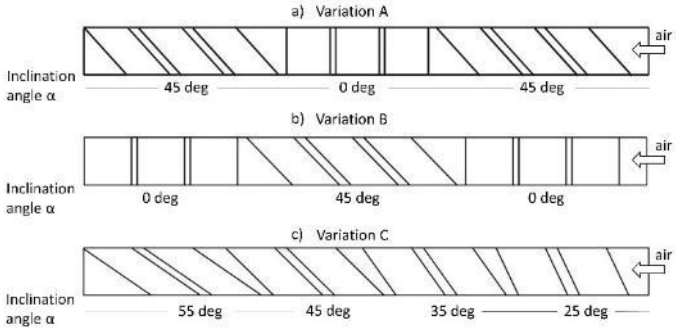

Figure 9. Variations to design able to achieve different profiles in the 3D-space: (a) Variation A (20.5 x 1.6 x 2) cm, (b) Variation B (19.3 x 1.6 x 2) cm, (c) Variation C (18.5 x 1.6 x 2) cm.

- A: 45^o, 0^o, 45^o - three cubes per angle,
- B: 0^o, 45^o, 0^o - three cubes per angle,
- C: 25^o, 35^o, 45^o, 55^o - two cubes per angle.

The profiles achieved by each variation to the original design were traced using the Vicon system by securing one marker on each of the customizable cubes of the actuators and recording their position at 0 kPa, 100kPa, 200kPa, and 300kPa. This is illustrated in Figure 10 (a-c), where the profile of the standard design at 300 kPa is included for comparison. Analysis shows that several bending modalities can be achieved upon combination of 2D- and 3D- bending, the latter being further customized by the inclination angle of each of the cubes which, as previously demonstrated, dictates the angular displacement and the radius of the helix. In summary, the geometries of the profiles obtained are as follows:

- A: helical – simple bending – helical,
- B: simple bending – helical – simple bending,
- C: heterogeneous helical motion,
- Standard design: homogeneous helical motion.

F. Design optimization

It has been shown that the maximum angular displacement ($337.21^o \pm 4.40^o$) was achieved by the actuator with inclination angle $\alpha = 45^o$ and cube side length $l = 3$cm. While the proposed design imposes no limit on the number of geometric parameters that could be varied to achieve the required motion kinematics, current 3D-printing technology restricts the inclination angle to $\alpha \leq 50^o$ to minimize the overhang, thus

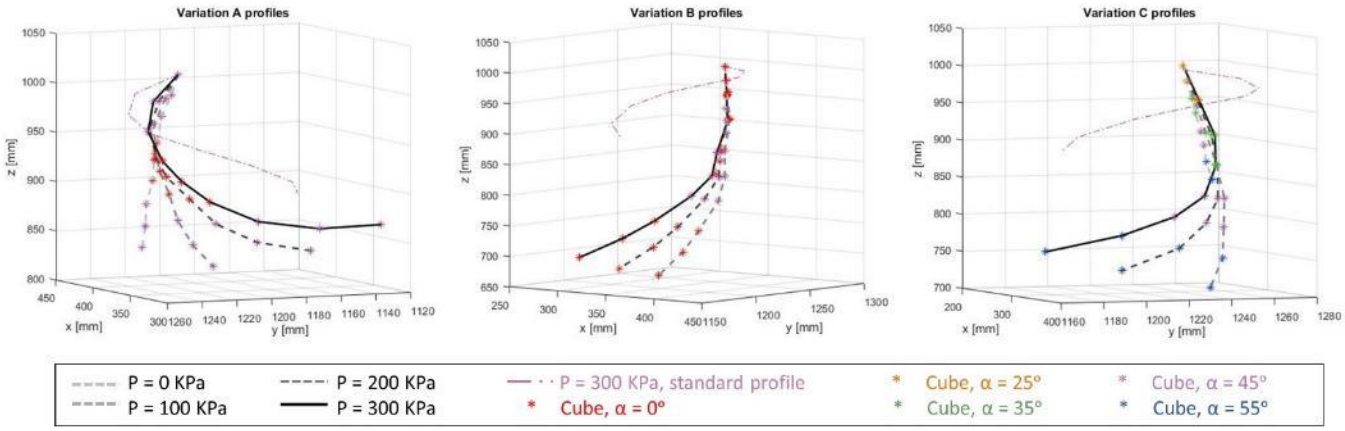

Figure 10 – Profiles achieved by the variation to the standard design, namely (a) helical-bending-helical profile, (b) bending-helical-bending profile, and (c) heterogeneous helical profile at 0, 100, 200, and 300 kPa. The profile of the standard design at 300 kPa is included for comparison.

risk of printing failure.

Design optimization could therefore be targeted by increasing the width and the height of the actuator to maximize the surface area of the frontal and back faces. This would, however, come at the expense of bulkiness which could be detrimental in a range of applications. Minimizing the wall thickness, the spacing between two adjacent cubes, and the cross-sectional area of the air channel connecting each pair of adjacent customizable cubes at the base is also believed to enhance performance. Furthermore, wherever possible, the total surface area of the customizable cubes is to be minimized as to reduce overhang during the fabrication process, the effects of gravity, and the overall bulkiness of the actuator.

V. Applications

The mechanical capabilities and the high degree of design customizability demonstrated in the sections above make the developed actuator suitable for a variety of applications. The usability of actuators capable of helical motion is now briefly demonstrated in the fields of object manipulation and rehabilitation engineering.

A. Object manipulation: knob

Due to their ability to achieve circular profiles, actuators capable of helical motion can enhance the quality of rotation in object-turning tasks. This is apparent in the case of a knob. While 2D-bending actuators can solely strike the handle and turn the knob by relying on the torque upon impact, the former is able to assist rotation allowing smoother motion.

This was demonstrated by rotating a 3D-printed solid knob with one FSR attached to the handle and connected to an Arduino microcontroller. The knob was then rotated by rapidly increasing the inflation pressure from 0kPa to 300kPa. Comparable designs capable of 2D-bending or helical motion ($\alpha = 45^{o}$, $l = 1.5$cm) were placed on the sensor and actuated as illustrated in Fig. 11(a). Fig. 11(b-e) depicts the relative position of the actuator with respect to the knob for the two actuator types, before and after actuation. The normalized striking force was measured and compared against the normalized spinning duration (Fig. 12). The graph clearly shows that the time of contact between the knob and the actuator is maximized by the actuator capable of helical motion, which moves along with the object to be rotated (98.67% vs. 20.67%). Instead, it is minimized by the bending actuator which strikes the object causing it to rotate unchecked and by a smaller angle (89.78^{o} vs. 150.18^{o}) than that achieved by the actuator capable of helical motion. The data were collected for three rotation cycles for averaging.

B. Object manipulation: gripper

The ability of our actuators to grasp objects upon exploitation of their 3D-bending motion is here demonstrated. Indeed, a gripper made with 3D-bending actuators can wrap around objects achieving a cylindrical contact profile, which results in a more secure grip than that attainable by an equal number of 2D-bending actuators. While it has been shown that configurations of four 2D-bending SPAs could be made to grasp and lift objects [17] [18], we demonstrate the ability to manipulate objects of a gripper composed of only two 3D-printed SPAs.

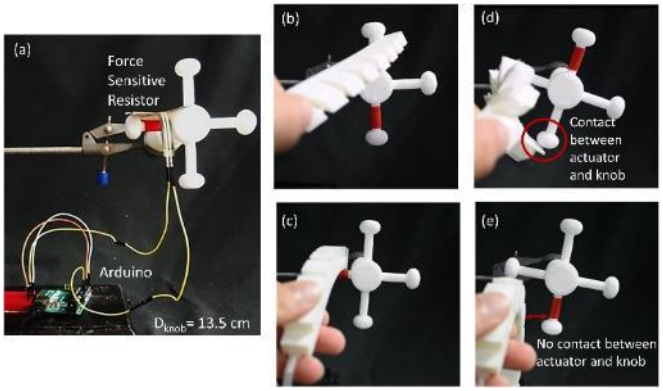

Figure 11. (a) Experimental setup to measure the contact between the actuator and the knob during rotation. Contact between (b) an actuator capable of helical motion and knob, and (c) bending actuator and knob, before actuation. Contact between (d) an actuator capable of helical motion and knob, and (e) bending actuator and knob, after actuation.

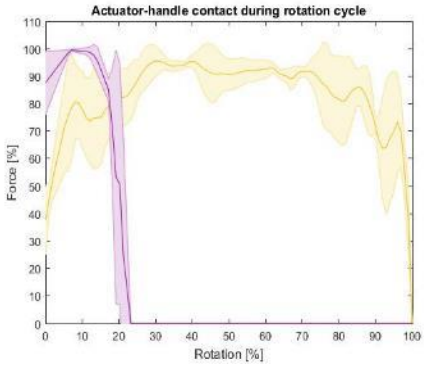

Figure 12. Actuator-handle contact during rotation cycle.

For this purpose, we secured two actuators ($\alpha = 45^{o}$, $l = 3.0$cm, 6 customizable cubes) to a simple 3D-printed support to grasp, lift, and manipulate ordinary objects. Actuated at 340kPa, the grip was secure and objects could be successfully rotated to any angle and maintained at any position. Fig. 13(a-c) shows the transferring of water from a bottle, a plastic container, and a plastic cup. The task was performed without any difficulty and was entirely repeatable.

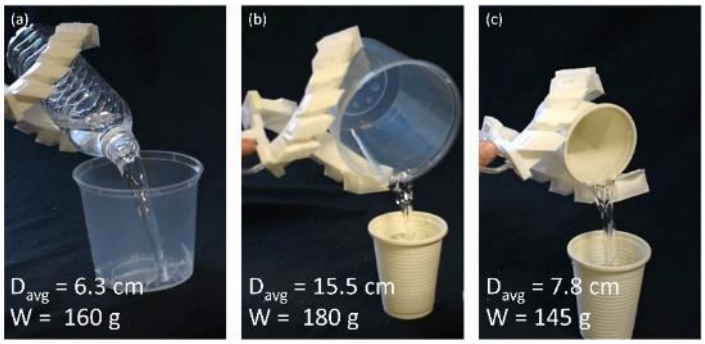

Figure 13. Gripping task involving pouring water (a) from a bottle to a container, (b) from a container to a cup, and (c) from a cup to a cup, including the average diameter and the weight of the objects being lifted.

C. Rehabilitation: thumb opposition

Our 3D-bending actuators have the potentials to aid in rehabilitation of the hand, and particularly in thumb opposition, which constitutes one of the most exacting rehabilitation exercises for individuals with hand disabilities. Indeed, due to the complexity of the thumb opposition (TMC) joint, most rehabilitation devices exclude the thumb from the exoskeleton [31], or limit rehabilitation to flexion/extension movements of the four fingers by adopting bending actuators only [17] [18]. While the silicon-based soft robotics glove developed by Polygerinos et al. [32] [33] successfully targets thumb opposition utilizing fiber-reinforced SPAs, the actuator presented in this work addresses the same issue, yet provides all the manufacturing advantages of 3D-printing technology.

The physiological path of the thumb during opposition has been compared to that achieved by means of an actuator capable of helical motion ($\alpha = 45^{o}$, $l = 3.0$ cm) using the Vicon system as in Fig. 14(a-b). The actuator was secured on the dorsal side of the thumb using flexible adaptors, and operated three times at 340kPa for each of the three trials performed. (72.70 ± 2.57) % of the physiological range of motion (ROM), defined as the angle between the tips of the little finger and the thumb formed with the CMC (59.27^{o}), was achieved. Finally, Fig. 15 shows that the trajectory traced in the 3D-space agrees with the physiological path of the joint during opposition.

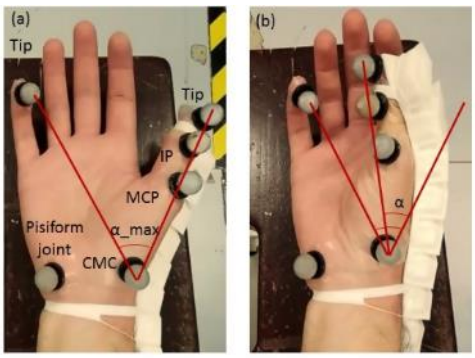

Figure 14. Experimental setup for thumb opposition experiment. (a) Maximum angle between the tip of the little finger, the CMC joint, and the tip of the thumb and (b) opposed position of the thumb during actuation.

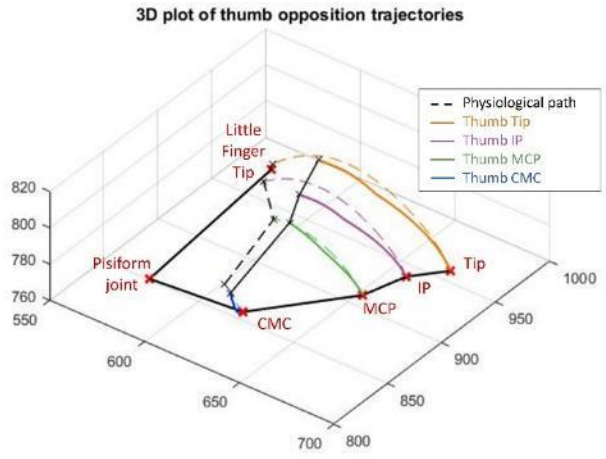

Figure 15. 3D-plot of the thumb trajectory during pressurization and comparison with physiological motion. All dimensions are in [mm].

VI. Conclusion

In this work, a novel design of SPAs based on customizable cubes at an angle with the longitudinal axis of the actuator has been presented. This was shown to enable 3D-printed SPAs, whose motion capabilities were previously restricted to planar bending, to achieve several 3D-bending modalities. The kinematic behavior of actuators capable of 2D-bending and of helical motion was therefore characterized by measuring the angular displacement and the bending radius, or that of the helix, at different pressures under static conditions. These results were validated by both analytical and FEA modelling. The output force of different designs at various poses was then obtained by means of a blocked force test. The high degree of geometry-based customizability was therefore demonstrated to be dependent upon the pattern of the inclination angle of the customizable cubes and on the surface area of the front and back faces. For controlling the angular displacement and the bending radius, or that of the helix, these geometric parameters are crucial in a variety of applications. Particularly, while the angular displacement determines the maximum obtainable rotation of a knob, the radius dictates the minimum size of the object that can be successfully grabbed and manipulated. Finally, for being capable of aiding in thumb opposition tasks, the actuator presented in this work has been demonstrated to open new possibilities in the field of printable wearable soft devices for rehabilitation,

Future work will focus on improving customizability by adopting a modular approach that would let the user adjust the inclination angle of each customizable cube to accomplish a particular bending profile. We also target actuator performance optimization by broadening the spectrum of flexible materials suitable for fused deposition modelling technology, and by developing new techniques to obviate overhang and other sources of printing failure.

VII. References

[1] Q. Shen, S. Trabia, T. Stalbaum,V. Palmre, K. Kim, I. Oh, "A multiple-shape memory polymer-metal composite actuator capable of programmable control, creating complex 3D motion of bending, twisting, and oscillation," *Scientific Reports,* 2016.

[2] J. M. Jani, M. Leary, A. Subic, M. A. Gibson, "A review of shape memory alloy research, applications and opportunities," *Materials and Design,* vol. 56, no. 5, pp. 1078-1113, 2014.

[3] W. C. Röntgen, "Ueber die durch Electricität bewirkten Form—und Volumenänderungen von dielectrischen Körpern," *Ann Phys Chem,* vol. 11, pp. 771-786, 1980.

[4] P. White, S. Latscha, M. Yim "Modeling of a Dielectric Elastomer Bender Actuator," *actuators,* vol. 3, pp. 245-269, 2014.

[5] H. S. Jung, S. Y. Yang, K. H. Cho, M. G. Song, C. T. Nguyen, H. Phung, U. Kim, H. Moon, J. C. Koo, J.-D. Nam, H. R. Choi, "Design and Fabrication of Twisted Monolithic Dielectric Elastomer Actuator," *International Journal of Control, Automation and Systems,* vol. 15, no. 1, pp. 23-35, 2017.

[6] S. Rosset, O. A. Araromi, S. Schlatter, H. R. Shea, "Fabrication Process of Silicone-based Dielectric Elastomer Actuators," *J Vis Exp,* vol. 108, 2016.

[7] R. Pelrine, R. Kornbluh, J. Joseph, R. Heydt, Q. Pei, S. Chiba, "High-field deformation of elastomeric dielectrics for actuators," *Materials Science and Engineering C,* vol. 11, pp. 89-100, 2000.

[8] D. Trivedi, A. Lotfi, C. D. Rahn, "Geometrically Exact Models for Soft Robotic Manipulators," *IEEE Transaction on Robotics,* vol. 24, no. 4, 2008.

[9] Y.-L. Park, J. Santos, K. G. Galloway, E. C. Goldfield, R. J. Wood, "A Soft Wearable Robotic Device for Active Knee Motions using Flat Pneumatic Artificial Muscles," *IEEE International Conference on Robotics & Automation (ICRA),* 2014 .

[10] B. Hannaford, C.-P. Chou, "Measurement and modeling of McKibben pneumatic artificial muscles," *IEEE Trans. Rob. Autom.,* vol. 12, no. 1, pp. 90-102, 1996.

[11] A. A. M. Faudzi, M. R. M. Razif, I. N. A. M. Nordin, K. Suzumori, S. Wakimoto, D. Hirooka, "Development of Bending Soft Actuator with Different Braided Angles," *The 2012 IEEE/ASME International Conference on Advanced Intelligent Mechatronics ,* 2012.

[12] B. Gorissena, T. Chishiroc, S. Shimomurac, D. Reynaerts, M. D. Volder, S. Konishi, "Flexible pneumatic twisting actuators and their application to tilting micromirrors," *Sensors and Actuators A: Physical,* vol. 216, pp. 426-431, 2014.

[13] Y. Sun, H. K. Yap, X. Liang, J. Guo, P. Qi, M. H. Jr. Ang, R. C. H. Yeow, "Stiffness Customization and Patterning for Property Modulation of Silicone-Based Soft Pneumatic Actuators," *Soft Robotics,* vol. 0, no. 0, 2017.

[14] P. Polygerinos, Z. Wang, K. C. Galloway, R. J. Wood, C. J. Walsh, "Soft robotic glove for combined assistance and at-home rehabilitation," *Robotics and Autonomous Systems,* vol. 73, p. 135–143, 2015.

[15] P. Polygerinos, Z. Wang, J. T. B. Overvelde, K. C. Galloway, R. J. Wood, K. Bertoldi, C. J. Walsh, "Modeling of Soft Fiber-Reinforced Bending Actuators," *IEEE Transaction on Robotics,* vol. 31, no. 3, 2015.

[16] A. Zolfagharian, A. Z. Kouzani, S. Y. Khoo, A. A. A. Moghadam, I. Gibson, A. Kaynak, "Evolution of 3D printed soft actuators," *Sensors and Actuators A: Physical,* p. 258–272, 2016.

[17] H. K. Yap, H. Y. Ng, R. C. H. Yeow, "High-Force Soft Printable Pneumatics for Soft Robotic Applications," *Soft Robotics,* vol. 3, no. 3, 2016.

[18] B. A. W. Keong, R. C. H. Yeow, "A Novel Fold-Based Design Approach towards Printable Soft Robotics using Flexible 3D Printing Materials," *Advanced Materials Technologies,* 2017.

[19] R.F. Natividad, M. R. D. Rosario, P. C.Y. Chen, R. C. H. Yeow, "A Hybrid Plastic-Fabric Soft Bending Actuator with Reconfigurable Bending Profiles," *IEEE International Conference on Robotics & Automation (ICRA),* 2017.

[20] O. H. Yeoh, "Some Forms of the Strain Energy Function for Rubber," *Rubber Chemistry and Technology,* vol. 66, no. 5, pp. 754-771, 1993.

[21] M. Rackl, "Curve Fitting for Ogden, Yeoh and Polynomial Models," *ScilabTEC, 7th International Scilab Users Conference,* 2015.

[22] J. Xiao, Z. Liu, Y. Yang, D. Liu, X. Han, "Comparison and Analysis of Indoor Wireless Positioning Techniques," *Computer Science and Service System (CSSS),* 2011.

[23] B. Carse, B. Meadows, R. Bowers, P. Rowe, "Affordable clinical gait analysis: An assessment of the marker tracking accuracy of a new low-cost optical 3D motion analysis system," in *Physiotherapy*, Elsevier, 2013, pp. 347-351.

[24] C. G. Fontanella, A. Forestiero, E. L. Carniel, A. N. Natali, "Analysis of heel pad tissues mechanics at the heel strike in bare and shod conditions," *Medical Engineering & Physics,* vol. 35, no. 4, pp. 441-447, 2013.

[25] R. A. R. C. Gopura, K. Kiguchi, E. Horikawa, "A Study on Human Upper-Limb Muscles Activities," *International Journal of Bioelectromagnetism,* vol. 12, no. 2, pp. 54-61, 2010.

[26] M. Valenti, B. Bethke, D. Dale, A. Frank, J. McGrew, S. Ahrens, J. P. How, J. Vian, "The MIT Indoor Multi-Vehicle Flight Testbed," *2007 IEEE International Conference on Robotics and Automation,* 2007.

[27] W. C. Young, R. G. Budynas, Roark's Formulas for Stress and Strain, McGraw-Hill, 2002, p. 508 (Table 11.4 8a).

[28] S. Timoshenko, J. M. Lessels, Applied Elasticity, Westinghouse Technical Night School Press, 1925.

[29] S. Timoshenko, S. W.- Krieger, Theory of Plates and Shells, McGraw-Hill, 1959.

[30] T. H. Evans, "Tables of Moments and Deflections for a Rectangular Plate Fixed at All Edges and Carrying a Uniformly Distributed Load," *ASME J. Appl. Mech.,* vol. 6, no. 1, 1939.

[31] Y. Chen, S. Le, Q. C. Tan, O. Lau, F. Wan, C. Song, "A Lobster-inspired Robotic Glove for Hand Rehabilitation," in *IEEE International Conference on Robotics and Automation (ICRA)*, Singapore, 2017 .

[32] P. Polygerinos, K. C. Galloway, E. Savage, M. Herman, K. O. Donnell, C. J. Walsh, "Soft Robotic Glove for Hand Rehabilitation and Task Specific Training," in *2015 IEEE International Conference on Robotics and Automation (ICRA)*, Seattle, Washington, 2015.

[33] F. Connolly, P. Polygerinos, C. J. Walsh, K. Bertoldi "Mechanical Programming of Soft Actuators by Varying Fiber Angle," *Soft Robotics,* vol. 2, no. 1, 2015.